Effect of substrate thermal properties on evaporating liquid hydrogen and ammonia spills

Martin Spillum Grønli, Hans Langva Skarsvåg*, Svend Tollak Munkejord

SINTEF Energy Research, P.O. Box 4761 Torgarden, NO-7465 Trondheim, Norway

---

Abstract

To decarbonize the energy, transport and industrial sectors, liquid hydrogen and ammonia are likely to be more widely employed. During an accidental release, these cryogens quickly spread and evaporate, producing explosive (H_2) or toxic (NH_3) clouds. Assessing the risks associated with storage and transport therefore requires tools that can simulate these spill processes, accounting for both the spill source, geometry and substrate thermal properties. In this work we have developed a flexible tool that takes the details of the spill, geometry and substrate as input. The parameters include initial spill velocity, ground topography, obstructions, and details regarding the thermal properties of the substrate. The latter includes temperature-dependent thermal properties, porosity and potential freeze out of trapped water. We validate this model against experimental data and apply it to relevant H_2 and NH_3 spill cases. Evaporation rates were found to vary significantly with substrate characteristics, and this is expected to have a large impact on safety distances.

Keywords: liquid hydrogen, liquid ammonia, spill modelling, safety, evaporation

---

1. Introduction

Hydrogen (H_2) and ammonia (NH_3) are expected to play an important role in the decarbonization of hard-to-abate sectors (van der Spek *et al.*, 2022). One of the challenges is their low energy density, which is mainly attributed to H_2 and NH_3 being in a gaseous state at standard conditions. The low energy density can be improved either by pressurization, or through a liquefaction process that takes the fluids to their liquid states at atmospheric pressure (−252.9 °C for H_2 and −33.34 °C for NH_3). For large-scale storage and long-distance seaborne transport, liquefaction is a main option (Berstad *et al.*, 2022).

There are risks related to the storage, transport and end use of all fuels. One must therefore be able to assess these risks for each specific application. Before LH_2 and LNH_3 are employed in larger quantities and/or in new applications, a thorough understanding of the possible hazardous scenarios is required. One of the scenarios that must be considered is the accidental release of the liquids. Determining where the spilled liquid flows, and how it evaporates, is important, both for hazards directly related to the liquid (frost damage to personnel or ignition) and for assessing the consequences of vapour dispersion in the atmosphere (risk of ignition and, in the case of NH_3, toxicity).

Several experiments have been conducted where LH_2 or LNH_3 is spilled on land, potentially leading to the formation of an evaporating pool. The primary objective of these experiments has been to understand the dispersion of H_2 (Witcofski and Chirivella, 1984; Statharas *et al.*, 2000; Willoughby and Royle, 2014; Hall, 2014; Aaneby *et al.*, 2021) and NH_3 (Dharmavaram *et al.*, 2023; McMasters and Fox, 2020) in gaseous form in the atmosphere.

---

*Corresponding author

Email address: `hans.skarsvag@sintef.no` (Hans Langva Skarsvåg)

In the 1980s, researchers from NASA conducted a series of seven experiments at the White Sands test site in New Mexico (Witcofski and Chirivella, 1984). The average spill rate for five of these tests was between 9.5 and 15 kg/s, considered to be large-scale experiments. The remaining two tests had an average spill rate of 4.7 kg/s and 0.8 kg/s. During the experiments, LH$_2$ was discharged by a helium back-pressure of 7 bar into a spill pond where it formed an evaporating pool on compacted sand. Test 6, which involved a liquid spill rate of $\dot{m}_\ell$ = 9.5 kg/s for a duration of 38 s, led to the formation of a pool with a radius between 2 and 3 m. This pool evaporated quickly once the spill ceased.

In the 1990s, Battelle Ingenieurtechnik for Bundesanstalt für Materialforschung und Prüfung (BAM) performed experiments where LH$_2$ was released between two buildings at a rate of around 0.4 kg/s during 2 minutes (Statharas *et al.*, 2000). The experiments were instrumented with sensors to measure pool size, ground temperature and evaporation behaviour. Unfortunately, the release rate is uncertain, especially because LH$_2$ was supplied through a 75 m long transfer line causing the liquid to heat and evaporate inside the pipe. An average liquid release rate of $\dot{m}_\ell$ = 0.37 kg/s was estimated.

In 2009–2011, the UK Health and Safety Laboratories (HSL) performed a series of tests in which unignited or ignited LH$_2$ was released at a rate of around 0.07 kg/s onto concrete (Willoughby and Royle, 2014; Hall, 2014). The purpose of the tests was to mimic a scenario where an LH$_2$ hose line fails during a tanker refuelling process. Three different orientations of the spill were investigated. Horizontal releases at a height of 0.86 m did not cause any pool formation. However, horizontal releases at ground level and vertical releases 0.1 m above the ground did result in a pool being formed.

In 2019 and 2020, the Norwegian Defence Research Establishment (FFI) performed seven outdoor and eight indoor LH$_2$ leakage tests, where liquid pool formation was part of the assessment (Aaneby *et al.*, 2021). Five of the seven outdoor tests were released vertically downwards 0.32 m above the ground with a release rate in the range 0.16–0.73 kg/s. The two other tests were released horizontally with a release rate of 0.83 kg/s. Only the vertical releases resulted in pool formation. The radius was limited to 0.5–1 m from the release source and the pool evaporated shortly after the releases were stopped. A new series of experiments involving the release of LH$_2$ was scheduled for 2023 at Sandia National Laboratories (Mangala Gitushi *et al.*, 2023).

Various computational tools (van den Bosch and Weterings, 2005; Verfondern and Dienhart, 1997; Holborn *et al.*, 2020) have been used to estimate the pool size for cryogenics, ranging from simple correlations for the radius to solving the shallow-water equations yielding a more precise description of the liquid flow. For the tools solving the shallow-water equations, several assumptions have typically been made to predict the pool evaporation rate. Firstly, the pools have been assumed to be in perfect thermal contact with the substrate. Moreover, the change in thermal properties as the substrate cools has not been accounted for. The latter may have a pronounced effect for cryogenic liquids such as LH$_2$, for which the ground is significantly cooled.

Most of the experiments available in the literature do not provide accurate data on pool sizes and evaporation rates. This makes it challenging to adequately validate computational tools designed to estimate these parameters. Nonetheless, efforts have been made in this direction. Assuming axisymmetric spills, Verfondern and Dienhart (1997) used the LachenAusbreitung-und-Verdampfung (LAuV) code, developed by Forschungszentrum Jülich (FZJ), to simulate NASA Test 6 (Witcofski and Chirivella, 1984). They predicted a maximum pool radius around twice as large as the experimentally reported one. The FLACS pool model is another tool that solves the shallow-water equations in order to predict the evaporation of a liquid pool. It was employed by Holborn *et al.* (2020) to predict the pool radius for several spill rates, including that in NASA Test 6. Relatively good agreement with the experimentally reported radius was observed. The model assumptions included perfect thermal contact between the liquid and substrate, and constant thermal properties of the substrate, despite the cooling of the ground. The same study indicated that changing substrate, i.e., changing thermal properties, can significantly influence the pool radius and evaporation rate. Thus, it can be anticipated that the cooling of the ground, causing a transient change in ground thermal properties, may have a similar significant impact.

In this work, we therefore solve the shallow-water equations governing the flow of the liquid while continuously accounting for the change in thermal properties of the ground as it is cooled by the
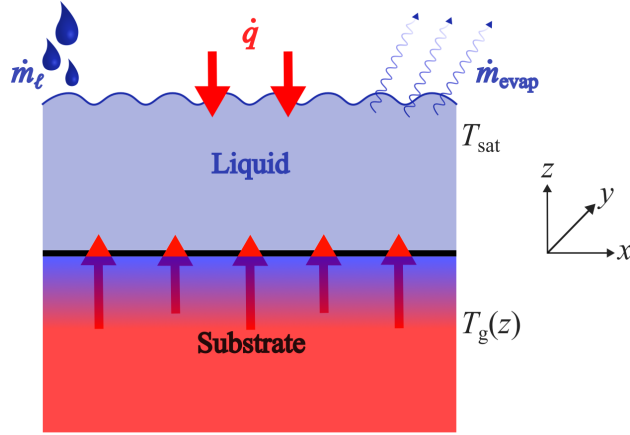
Figure 1: Sketch of evaporation model.

cryogenic liquid. This allows us to determine if the assumption of constant thermal properties is adequate. Furthermore, we investigate the validity of the assumption of perfect thermal contact between the liquid and the substrate. This is particularly interesting to examine for both LH_2 and LNH_3, since the two liquids typically have different boiling characteristics. The tool that has been developed, building on an open-source code, is freely available on Github (Grønli *et al.*, 2024). It is capable of simulating time-dependent spills of any shape with a nonzero initial velocity. Additionally, obstacles of varying shape and height may be included.

The rest of this article is organized as follows. Section 2 introduces the methodology to predict the spreading and continuous evaporation of LH_2 and LNH_3. Section 3 discusses the effect of variable ground thermal properties, ground moisture, and heat transfer assumptions. Also, a geometrically more complex case showing the versatility of the model is considered. Section 4 provides concluding remarks.

2. Method

In the following, we present a method that predicts the spreading and continuous evaporation of LH_2 or LNH_3 on solid ground subsequent to a containment breach, see Fig. 1. Generally, a cryogenic liquid spill will spread across the ground surface while being heated by both the substrate and the atmosphere, leading to evaporation into the atmosphere. The approach is divided into two consecutive steps: (1) Solve the 1D heat equation to obtain the heat flux from the ground into the liquid, $\dot{q}_g = \dot{q}_g(t_w)$, where $t_w(x, y)$ is the time a ground grid cell has been wet; (2) Solve the shallow-water equations to calculate the spreading and evaporation of the liquid.

In the second step, the ground heat flux obtained from the first step is utilized as input to determine the local evaporation rate. This one-way coupling approach disregards horizontal temperature gradients in the ground, yielding a heat flux solely dependent on the duration the ground grid cells have been covered by cold liquid, t_w. This should be a good approximation, as thermal gradients are in the range of $10\,\mathrm{K\,cm^{-1}}$ to $100\,\mathrm{K\,cm^{-1}}$ (e.g., shown in Fig. 3), while horizontal thermal gradients are determined by length scales of the spill (several meters). The computational cost saved by this exploitation of the underlying physics, and avoiding a 3D heat conduction problem with variable thermal properties, reduced the problem from completely unfeasible to a single 1D-simulation pre-processing calculation. This pre-processing step, depending on the complexity of the thermal properties, is done in the range of minutes to an hour. The following spill simulation time is some minutes. This also means that doing variations of geometry and spill source is fast if the substrate stays the same.

In case of an accidental release of LH_2 or LNH_3, the size and local evaporation rate predicted here are important input parameters to dispersion analysis of NH_3 and H_2 in the atmosphere (see e.g., Skarsvåg

et al. (2024)). Allowing for temperature-dependent ground properties facilitates a detailed examination of the types of substrates that yield the least hazardous pool size and evaporation rate for a given spill scenario.

Before presenting the results for different thermal properties and substrates such as dry or wet sand, and dry or wet concrete, we describe the details of the two-step model.

2.1. Pool spreading

In this work we have developed a new tool (Grønli *et al.*, 2024) building on the Conservation Laws Package (Clawpack) (Clawpack Development Team, 2022) to simulate the spill and spreading of LH$_2$ and LNH$_3$ on solid ground. Spreading of the liquid is modelled by solving the shallow-water equations on a two-dimensional Cartesian grid. The shallow-water equations are a set of hyperbolic partial differential equations derived from depth-integrating the Navier-Stokes equations, assuming that the horizontal length scale is much larger than the vertical length scale.

The first equation, derived from conservation of mass, reads

$$(h)_t + (hu)_x + (hv)_y = \frac{\dot{m}_\ell - \dot{m}_{\text{evap}}}{\rho_\ell}, \tag{1}$$

in which h is the spill height (m), u, v are the velocities (m/s) in the x- and y-direction, $\dot{m}_\ell$, $\dot{m}_{\text{evap}}$ are the liquid mass spill and evaporation rates per unit area (kg/m^2 s), and ρ_ℓ is the liquid density (kg/m^3). Given a liquid-mass spill rate $\dot{m}_\ell$, the height at points in space where the liquid is spilled will increase at a rate (m/s)

$$\dot{h}_\ell(x, y, t) = \frac{\dot{m}_\ell(x, y, t)}{\rho_\ell}. \tag{2}$$

Similarly, at a given evaporation rate $\dot{m}_{\text{evap}}$, the height will decrease at a rate

$$\dot{h}_{\text{evap}}(x, y, t) = \frac{\dot{m}_{\text{evap}}(x, y, t)}{\rho_\ell}. \tag{3}$$

The two remaining shallow-water equations, derived from conservation of momentum, are

$$(hu)_t + (hu^2 + \frac{1}{2}gh^2)_x + (huv)_y = -\gamma(hu) - ghb_x, \tag{4}$$

$$(hv)_t + (hv^2 + \frac{1}{2}gh^2)_y + (huv)_x = -\gamma(hv) - ghb_y, \tag{5}$$

where g is the gravitational acceleration (m/s^2). The first source term on the right-hand side of both equations is a Manning friction term that includes the effect of substrate friction. The variable γ is given by

$$\gamma = \frac{gn^2 \sqrt{(hu)^2 + (hv)^2}}{h^{7/3}}, \tag{6}$$

where the Manning coefficient n (s/m$^{1/3}$) is correlated with ground surface roughness (The Engineering ToolBox, 2004). Next, the last term on the right-hand side of Eqs. (4) and (5) defines the topography where a nonzero elevation of the ground, b (m), is allowed. This is used to introduce obstacles or confinements of arbitrary shapes, such as dikes.

The shallow-water equations (1), (4) and (5) are solved by Clawpack (Clawpack Development Team, 2022) which is a collection of finite-volume methods for linear and nonlinear hyperbolic systems of conservation laws written in Fortran and Python. More specifically, we use the Python interface PyClaw together with a SharpClaw solver that provides high-order wave propagation using WENO (weighted essentially non-oscillatory) or TVD (total variation diminishing) reconstruction and Runge-Kutta time integration (Ketcheson *et al.*, 2013). The SharpClaw solver is selected as it tackles dry states where $h = 0$.

In this work we have modified PyClaw such that spills can be instantaneous (dam-break) or continuous, having a time-dependent spill rate. Various spill sizes and shapes, along with the option to assign a nonzero horizontal velocity, are also possible. For instance, for a spill rate $\dot{m}_\ell$ with an initial velocity u_0 in the x-direction, the resulting velocity in the x-direction within the spill domain becomes

$$u' = \frac{u_0 \dot{m}_\ell \Delta t + u m_\ell}{\dot{m}_\ell \Delta t + m_\ell}, \tag{7}$$

where m_ℓ denotes the mass of liquid already present inside the spill domain and Δt is the time step used in PyClaw.

2.2. Heat conduction and evaporation

The liquid mass evaporation rate in shallow-water equation (1) can be estimated through the relation

$$\dot{m}_{\text{evap}} = \frac{\dot{q}}{\Delta H_{\text{evap},\ell}}, \tag{8}$$

in which $\dot{q}$ is the heat flux into the pool per unit area (W/m^2) and $\Delta H_{\text{evap},\ell}$ is the liquid heat of evaporation at atmospheric pressure (J/kg). The liquid is assumed to stay at a saturated liquid state until complete boil-off, i.e., the liquid temperature $T_\ell = T_{\text{sat}}$, where T_{sat} is the saturation temperature. Evaporation is caused by heating from the ground and air at rates $\dot{q}_\text{g}$ and $\dot{q}_\text{a}$, respectively. Other heat fluxes such as radiation to and from the atmosphere are neglected as these are small (Verfondern and Dienhart, 1997), at least during the initial stages of evaporation. Thus, the total heat flux into the pool is $\dot{q} = \dot{q}_\text{g} + \dot{q}_\text{a}$.

The heat flux from the air is given by

$$\dot{q}_\text{a} = k_\text{a}(T_\text{a} - T_\ell), \tag{9}$$

where T_a is the temperature of the atmosphere (K) and the heat transfer coefficient, k_a (W/m^2 K), is estimated by assuming turbulent flow over a flat plat such that

$$k_\text{a} = \begin{cases} \dfrac{\text{Nu}\lambda_\text{a}}{2r_\text{p}} = \dfrac{0.037 \text{Pr}_\text{a}^{1/3}\text{Re}^{0.8}\lambda_\text{a}}{2r_\text{p}} & \text{if } r_\text{p} \geq 0.1\,\text{m} \\ 0 & \text{if } r_\text{p} < 0.1\,\text{m} \end{cases} \tag{10}$$

in which r_p is the radius of the liquid pool (m), Pr_a is the Prandtl number of air (-) and λ_a is the thermal conductivity of air (W/m K) (van den Bosch and Weterings, 2005). The Reynolds number is given by

$$\text{Re} = \frac{\rho_\text{a} u_{\text{a},10} \cdot 2r_\text{p}}{\eta_\text{a}}, \tag{11}$$

for which ρ_a is the density of air (kg/m^3), $u_{\text{a},10}$ is the wind speed at 10 m height (m/s) and η_a is the dynamic viscosity of air (kg/m s).

The dominant contribution to evaporation is the ground heat flux, $\dot{q}_\text{g}$. We expect vertical gradients in ground temperature to be much larger than horizontal temperature gradients. Thus, we can disregard heat transport in the horizontal directions and employ a 1D heat-transfer model. Hence, the heat flux from the ground is solely determined by the duration for which the ground remains covered by liquid. The temperature profile in the ground is given by the 1D heat equation

$$\frac{\partial}{\partial z}\left(\lambda_\text{g}\frac{\partial T_\text{g}}{\partial z}\right) = \rho_\text{g} c_{\text{p},\text{g}}\frac{\partial T_\text{g}}{\partial t}, \tag{12}$$

where λ_g, ρ_g and $c_{\text{p},\text{g}}$ are the ground thermal conductivity, density and specific heat capacity (J/kg K), respectively.

A simple approach is to assume temperature-independent (constant) properties λ_g, ρ_g and $c_{p,g}$ along with perfect thermal contact between the ground and the liquid pool. The resulting heat equation (12) can be solved analytically and the ground heat flux is then given by

$$\dot{q}_g = \frac{\lambda_g \left(T_g^\infty - T_\ell \right)}{\sqrt{\pi \alpha_g t_w}}, \tag{13}$$

where λ_g and α_g are the constant thermal conductivity and diffusivity (m^2/s) of the ground. Moreover, T_g^∞ is the ground temperature at infinite depth and t_w is the time the ground has been wet.

However, as this is potentially too simplistic, we have tested the effect of accounting for temperature-dependent (variable) thermal properties λ_g, ρ_g and $c_{p,g}$, along with the distinct boiling regimes experienced by LNH$_3$ and LH$_2$. Hence, Eq. (12) is solved numerically utilizing the Python library pyPDE (Jackson, 2019). Among the substrates that have been considered are dry and wet saturated sand. The thermal conductivity of saturated wet soil can be approximated by

$$\lambda_{g,\text{sat(u)}} = \lambda_s^{1-n_u} \lambda_{w(u)}^{n_u}, \tag{14}$$

where λ_s and $\lambda_{w(u)}$ are the thermal conductivities of solid particles (quartz) and unfrozen water, respectively, while the porosity of the unfrozen soil is set to $n_u = 0.335$ m^3/m^3 (Côté and Konrad, 2005a). Due to the low temperatures of LNH$_3$ and LH$_2$, soil containing water will freeze as it is cooled. The thermal conductivity of frozen saturated soil is calculated by

$$\lambda_{g,\text{sat(f)}} = \lambda_s^{1-n_f} \lambda_{w(f)}^{n_f}, \tag{15}$$

in which $\lambda_{w(f)}$ is the thermal conductivity of frozen water and n_f is the porosity of frozen soil. Côté and Konrad (2005b) estimated a 9 % volume increase as pore water freezes to ice, implying a frozen porosity $n_f = 1.09 n_u / (1 + 0.09 n_u)$. The effect of the transition from unfrozen to frozen saturated soil on thermal conductivity has been modelled by

$$
\begin{aligned}
\lambda_{g,\text{sat}}(T) = & \frac{1}{2} \left[1 + \tanh \beta (T - 271.15 \text{ K}) \right] \lambda_{g,\text{sat(u)}}(T) \\
& + \frac{1}{2} \left[1 - \tanh \beta (T - 271.15 \text{ K}) \right] \lambda_{g,\text{sat(f)}}(T),
\end{aligned} \tag{16}
$$

where β is a parameter with unit 1/K controlling how fast the transition occurs. Here, we have assumed 2 K subcooling and neglected any significant freezing point depression. The same model has been applied to dry sand with air filling the pores instead of water, yielding a thermal conductivity $\lambda_{g,\text{dry}} = \lambda_s^{1-n_u} \lambda_a^{n_u}$ where λ_a is the thermal conductivity of air. Herein, we have assumed that condensation of air components, which could occur for LH$_2$ spills, has a limited influence on the spill-evaporation dynamics. Numerical values for thermal conductivity have been obtained from Dincer and Zamfirescu (2015); Carnahan *et al.* (2021); Simoncelli *et al.* (2023); Kadoya *et al.* (1985); Dahmani *et al.* (2007) and are plotted in Fig. 2a for different substrates.

The specific heat capacity is assumed to equal the mass-weighted sum of the specific heat capacities for each constituent (quartz and water/air). For wet sand we must account for the freezing of ground moisture. The individual specific heat capacities of unfrozen (u) and frozen (f) wet sand read

$$c_{p(u)}(T) = w_u c_{p,w(u)}(T) + (1 - w_u) c_{p,s}(T), \tag{17}$$

$$c_{p(f)}(T) = w_f c_{p,w(f)}(T) + (1 - w_f) c_{p,s}(T), \tag{18}$$

where $c_{p,w(u)}$, $c_{p,w(f)}$ and $c_{p,s}$ are the specific heat capacities of unfrozen water, frozen water and quartz, respectively. The water content (% by weight) is $w_u = S_r n_u \rho_{w(u)} / (\rho_s (1 - n_u))$ for the unfrozen state and $w_f = S_r n_f \rho_{w(f)} / (\rho_s (1 - n_f))$ for the frozen state. Here, S_r is the degree of saturation, ρ_s is the density of quartz and $\rho_{w(u)}$, $\rho_{w(f)}$ are the densities of unfrozen and frozen water, respectively.

6
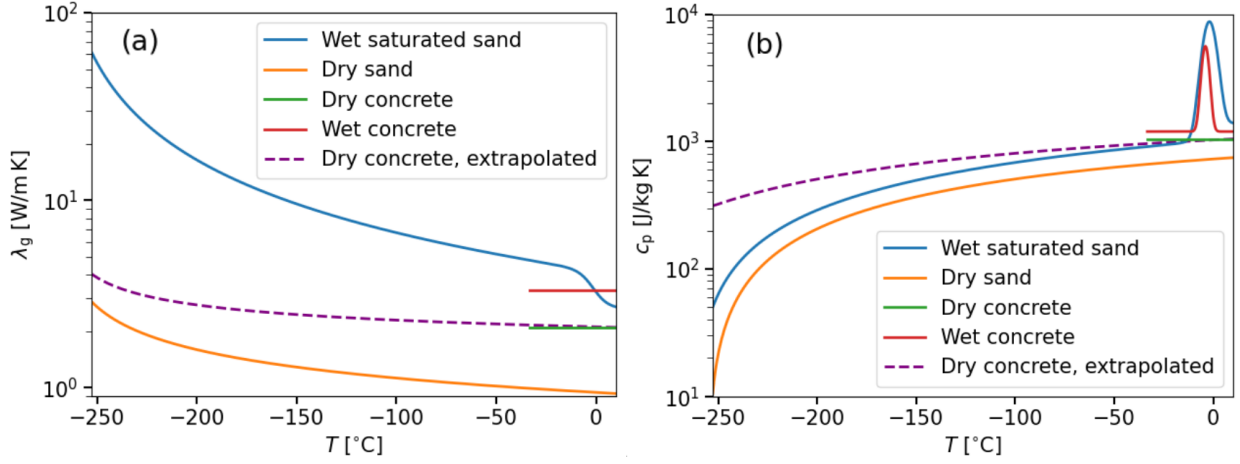
Figure 2: Thermal conductivity λ_g (a) and effective specific heat capacity c_p^{eff} (b) of different substrates.

With Eqs. (17) and (18), the specific heat capacity of wet saturated sand can be modelled in the same way as thermal conductivity in Eq. (16). However, due to freezing of ground moisture we add the heat of solidification of water, $\Delta H_{\text{sol,w}}$, through a sharp Gaussian distribution with standard deviation $\sigma \approx 1/\beta$. This yields an effective specific heat capacity of wet saturated sand

$$
\begin{aligned}
c_p^{\text{eff}} = {} & \frac{1}{2} \left[1 + \tanh \beta (T - 271.15 \text{ K}) \right] c_{\text{p(u)}}(T) \\
& + \frac{1}{2} \left[1 - \tanh \beta (T - 271.15 \text{ K}) \right] c_{\text{p(f)}}(T) \\
& + \frac{w_{\text{u}} \Delta H_{\text{sol,w}}}{\sigma \sqrt{2\pi}} \exp \left\{ -\frac{1}{2} \frac{(T - 271.15 \text{ K})^2}{\sigma^2} \right\}.
\end{aligned}
\tag{19}
$$

Note that if the substrate is rapidly cooled from above the freezing point to well below, the released energy shows little sensitivity to the magnitude of σ. Numerical values for specific heat capacity have been found in Lemmon *et al.* (2024, 2000); Harvey (2019) and are plotted in Fig. 2b, where the parameter σ has been set to 3.33.

In Figs. 2a and 2b, the thermal properties of concrete have also been plotted. These have not been calculated from the above equations but directly obtained from Dahmani *et al.* (2007). Here, the experimentally determined thermal properties of wet concrete are given for concrete that was first dried and then wetted (i.e., rewetted). These data were only available at temperatures relevant to LNH$_3$ spills. To illustrate the effect of variable thermal properties for dry concrete, we extrapolate the constant values (dashed lines in Figs. 2a and 2b). In doing so, we assume the same temperature dependency as for dry sand, offset by the values at $10\,^\circ$C for dry concrete. These extrapolated values are only used in Section 3.1.1.

It is observed that the ground density, whether in the unfrozen state, $\rho_{\text{g(u)}}$, or the frozen state, $\rho_{\text{g(f)}}$, exhibits minimal variation with changes in temperature. Hence, both are assigned a constant value that represents a weighted average of each component in the ground. However, for dry sand, the temperature dependence of air density, ρ_{a}, is accounted for by assuming ideal gas behaviour.

Assuming perfect thermal contact between ground surface and liquid as in Eq. (13) gives the maximal possible ground heat flux, $\dot{q}_g$. However, the heat flux will be limited by the boiling regime. This is governed by the temperature difference $\Delta T_{g\ell} \equiv T_g^0 - T_\ell$, where T_g^0 is the ground surface temperature. For ground temperatures above the Leidenfrost temperature, T_{L}, the cryogen will film boil. The Leidenfrost temperature can be estimated by the expression $T_{\text{L}} = 27 T_{\text{c}}/32$, where T_{c} is the critical temperature of the fluid (Spiegler *et al.*, 1963). We find $T_{\text{L}}^{\text{H}_2} = 28\,\text{K}$ for H$_2$ and $T_{\text{L}}^{\text{NH}_3} = 342\,\text{K}$ for

NH_3. This means that initially H_2 will always film boil, while NH_3 will be in the nucleate boiling regime.

For LH_2 boiling on flat horizontal surfaces it is recommended by Baldwin *et al.* (2021) to use Klimenko's film boiling correlation (Klimenko and Shelepen, 1982). Hence, the ground heat flux for boiling LH_2 reads

$$\dot{q}_{g,H_2} = \begin{cases} 0.19\Delta T_{g\ell}\lambda_\ell B^{0.333}\mathrm{Pr}_v^{0.333}f_1(K)/\lambda_{cr} & \text{if } B < 10^8 \\ 0.0086\Delta T_{g\ell}\lambda_\ell B^{0.5}\mathrm{Pr}_v^{0.333}f_2(K)/\lambda_{cr} & \text{if } B > 10^8, \end{cases} \tag{20}$$

where λ_ℓ is the thermal conductivity of LH_2 and Pr_v is the Prandtl number of the vapour film formed between the ground surface and the liquid. Further, B is a variable given by

$$B = \frac{\lambda_{cr}^3 g}{\nu_v^2}\left(\frac{\rho_\ell}{\rho_v} - 1\right), \tag{21}$$

in which the critical (Laplace) length scale, λ_{cr} (m) is

$$\lambda_{cr} = 2\pi\sqrt{\frac{\sigma_\ell}{g(\rho_\ell - \rho_v)}}. \tag{22}$$

Herein, σ_ℓ is the surface tension (N/m), ρ_v is the vapour film density and ν_v is the kinematic viscosity of the vapour film (m^2/s). Moreover, in Eq. (20) we have

$$f_1(K) = \begin{cases} 1 & \text{if } K \leq 1.4 \\ 0.89K^{0.333} & \text{if } K > 1.4 \end{cases} \tag{23}$$

and

$$f_2(K) = \begin{cases} 1 & \text{if } K \leq 2 \\ 0.71K^{0.5} & \text{if } K > 2, \end{cases} \tag{24}$$

where

$$K = \frac{\Delta H_{evap,\ell}}{c_{p,v}\Delta T_{g\ell}}. \tag{25}$$

All vapour film properties (v), such as the specific heat capacity of the vapour film, $c_{p,v}$, are evaluated at the vapour film temperature estimated as $T_v = (T_\ell + T_g^0)/2$ (Sciance, 1966). The vapour film acts as an insulator which considerably decreases the heat flux compared to a nucleate boiling regime. Liquid properties (ℓ) are evaluated at the liquid temperature $T_\ell = T_{sat}$.

For LNH_3 we impose Mostinski's nucleate boiling correlation (Mostinski, 1963)

$$\dot{q}_{g,NH_3} = 1.167 \cdot 10^{-8}p_{crit}^{2.3}F_{PF}^{10/3}\Delta T_{g\ell}^{10/3} \tag{26}$$

as a boundary condition to Eq. (12). Here, p_{crit} is the critical pressure of LNH_3 given in kPa. Moreover, F_{PF} is a non-dimensional pressure correction factor that characterizes pressure effects on nucleate boiling as

$$F_{PF} = 1.8p_r^{0.17} + 4p_r^{1.2} + 10p_r^{10}, \tag{27}$$

in which $p_r = p/p_{crit}$ is the reduced ambient pressure (-) where we assume atmospheric pressure, $p = p_a$ (Pa).

The heat flux calculated by Eq. (20) for LH_2 or Eq. (26) for LNH_3 will then serve as an input to shallow-water equation (1) via Eq. (8). The resulting temperature profiles for different substrates being covered by LH_2 after 100 s are plotted in Fig. 3. Here we see the significant impact of moisture in the ground: dry sand has the lowest heat capacity and is thus cooled more easily, while wet sand can release much more heat without the same cooling, due to increased heat capacity and latent heat. Note that it is the surface temperature that determines the heat transfer to the LH_2. Due to decreased ground surface temperature, a possible transition to natural convection for LNH_3 and transition boiling for LH_2 can be expected for longer simulations than those we have run here.
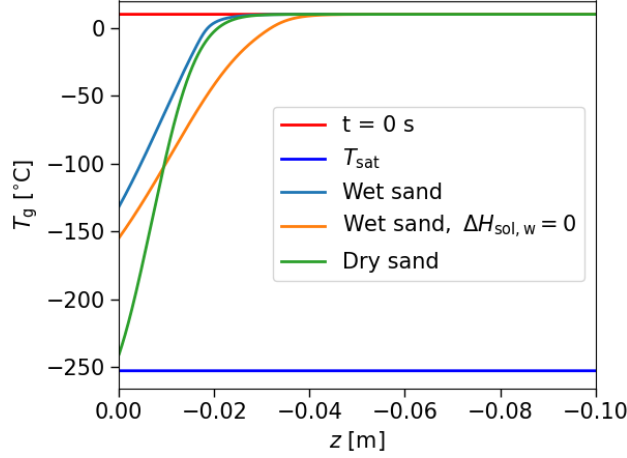
Figure 3: Temperature profiles in sand covered by LH$_2$ after 100 s. "Wet sand, $\Delta H_{sol,w} = 0$" denotes that the heat of solidification is excluded. Variable thermal properties and boiling correlations are used with an initial ground temperature $T_g(t = 0) = 10\,°C$.

3. Results and discussion

In the following, we examine how the thermal properties of the substrate, as well as the contact between liquid and substrate affect liquid spreading and evaporation rate. Firstly, we validate our tool by comparing the ground temperature from our simulations with experimental data for LH$_2$ provided by the Norwegian Defence Research Establishment (FFI) (Aaneby et al., 2021). The temperature profile in the ground primarily determines the heat flux, which significantly influences the evaporation rate. Next, our tool is validated against experimental data from NASA Test 6 (Witcofski and Chirivella, 1984) and compared to FLACS pool model results (Holborn et al., 2020). Subsequently, we conduct a case study to examine the effect of accounting for the temperature dependency of ground thermal properties. Moreover, we discuss the assumption of perfect thermal contact between the liquid and substrate by employing boiling correlations. Finally, the case study assesses the effect of moisture in the ground for sand and concrete.

The pool spreading is simulated using PyClaw on a 2D grid with a grid spacing and time step Δt, satisfying a maximal CFL (Courant–Friedrichs–Lewy) number of 0.9. The numerical parameters are summarized in Table 1, where "dry tolerance" refers to the maximal height h at which the substrate is considered to be dry. As the pool approaches complete boil-off and becomes increasingly shallow, the radius could be particularly sensitive to this parameter. In the same table, the grid spacing and time-step length for solving the heat equation (12) in Python are given.

Table 2 lists the main physical parameters. Herein, the Manning coefficient n, controlling the bottom friction, is set to 0.018 s/m$^{1/3}$ (The Engineering ToolBox, 2004). All spills are centred at $(x, y) = (0, 0)$ with zero initial velocities u_0, v_0, unless otherwise stated. For all cases in the case study, the initial ground temperature is $T_g^0 = 10\,°C$ and the air temperature is $T_a = 10\,°C$. Moreover, the wind speed at 10 m height is $u_{a,10} = 2$ m/s, while the liquid temperature is $T_\ell = T_{sat}$. Thermodynamic and transport properties of LH$_2$, LNH$_3$ and water are obtained from the NIST Webbook (Lemmon et al., 2024) or using Thermopack with NIST-MEOS as equation of state (Wilhelmsen et al., 2017).

3.1. Validation against experiments

In this subsection, we validate our tool against the experiments conducted by FFI and NASA, described in Section 1, and compare it to FLACS pool model results.
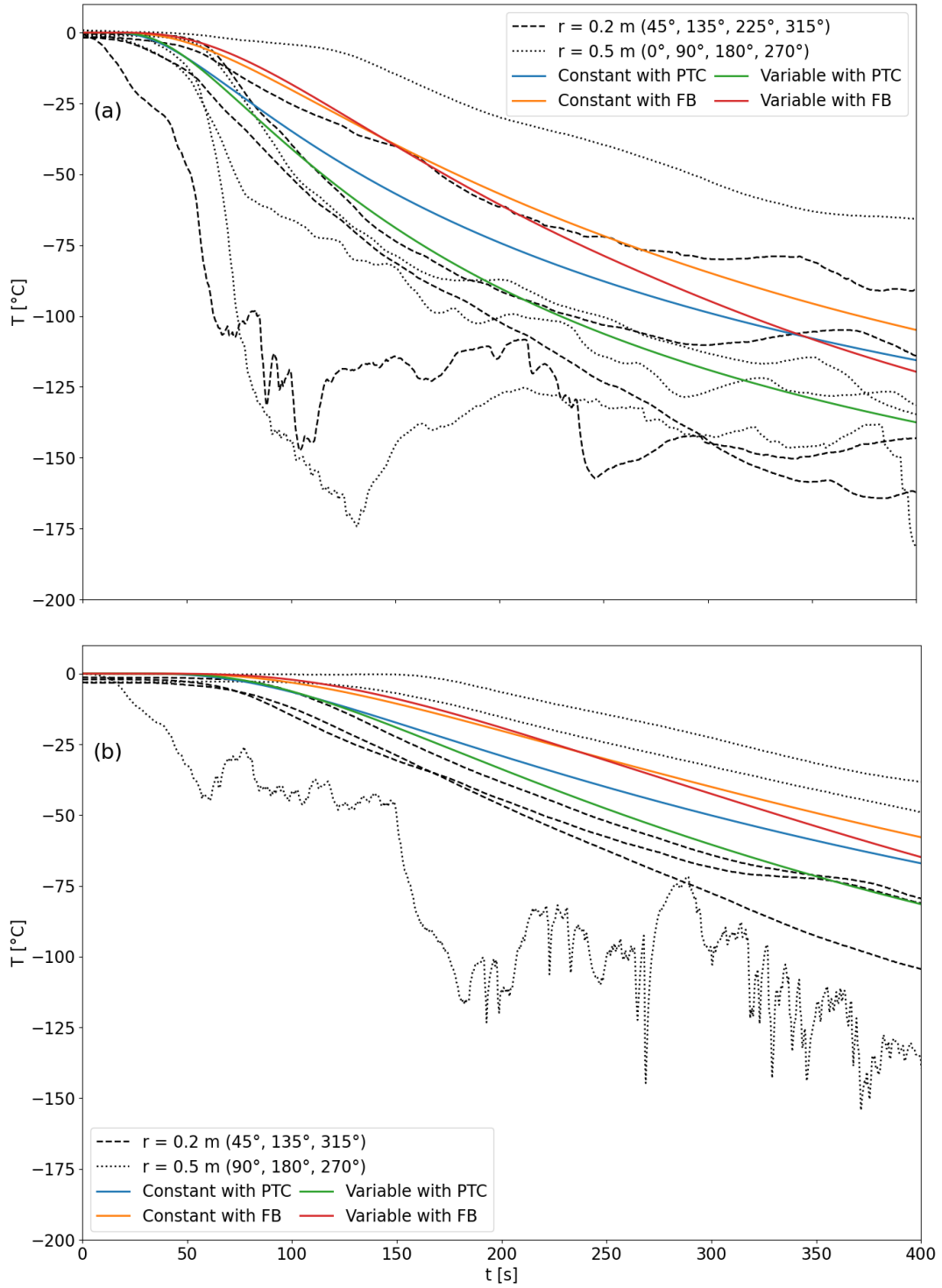
Figure 4: Validation against FFI experiments. Temperature as a function of time in concrete covered by LH$_2$ at a depth of $z = 20$ mm and $z = 30$ mm in (a) and (b), respectively. Black curves represent experimentally recorded values at different radii r from the spill point and at different angles around it. Full lines are calculated with constant or variable properties, and perfect thermal contact (PTC) or film boiling (FB).

Table 1: Numerical parameters.

Variable	Value
Grid spacing for pool spreading	10^{-2} m
Max. CFL number for pool spreading	0.9
Dry tolerance for pool spreading	10^{-5} m
Grid spacing for heat equation	$5 \cdot 10^{-5}$ m
Time step for heat equation	10^{-5} s
Parameter in Eq. (19), σ	$[3.33, 7.33]$ K

Table 2: Physical parameters.

Variable	Value
Manning coefficient n	0.018 s/m$^{1/3}$
Unfrozen porosity of sand n_{u}	0.335
Degree of saturation for wet sand S_{r}	1
Initial ground temperature T_{g}^0 in Section 3.1.1	0 °C
Initial ground temperature T_{g}^0 in Section 3.2	10 °C
Air temperature T_{a}	10 °C
Wind speed at 10 meters height $u_{\mathrm{a},10}$	2 m/s
Density of quartz	2650 kg/m^3
Density of concrete	2200 kg/m^3

3.1.1. Validation against FFI experiments

In the experiments conducted by FFI, LH$_2$ was released onto concrete (Aaneby *et al.*, 2021). Thermocouples were used to measure the ground temperature at depths of 20 mm and 30 mm and radii of 0.2 m and 0.5 m from the spill source, at various angles around it. Figs. 4a and 4b display the ground temperatures calculated by our model alongside the experimentally reported temperatures for Test 7. Test 7 involved a vertical downward release with a mass outflow rate of 0.16 kg/s over 8 minutes and an LH$_2$-tanker pressure of 0.8 barg. As seen in Figs. 4a and 4b, the experimental values vary significantly with the angle around the spill source. The variations may be explained by the difficulty of measuring such low temperatures, the potential of inaccuracies in thermocouple placement at the specified depths and LH$_2$ penetration into the ground, as suggested in Aaneby *et al.* (2021).

The experimental values are compared to our model, which is run with both constant and variable thermal properties, and under the assumption of perfect thermal contact or film boiling. Since thermal properties are unavailable for concrete at low temperatures, we assume that the thermal properties of dry concrete have the same temperature dependency as for dry sand, offset by the values at 10 °C for dry concrete, as shown in Figs. 2a and 2b. The ground temperatures calculated by our model all fall within the range of the experimentally measured temperatures. However, it can be seen that the scatter in the experimental data is in the order of the deviation between the data and the simulations. Overall, accounting for the variability in ground thermal properties gives better agreement with the experimentally observed temperatures. Interestingly, assuming perfect thermal contact aligns more closely with the experimental data than the film-boiling assumption. This could be explained by an under-prediction of the heat transfer by the film-boiling correlation, which could be due to the effects of the LH$_2$ flow and the rough surface. Some uncertainty also comes from the temperature dependence of the thermal properties, which can be seen by the significant difference between the constant thermal properties case and that of the variable properties in Fig. 4.

3.1.2. Validation against NASA experiments and comparison to FLACS simulations

In Fig. 5, the experimentally reported pool radius is indicated for NASA Test 6, having a spill rate $\dot{m}_\ell = 9.5$ kg/s and duration of 38 s. The pool was observed to have a radius between 2 and 3 m, and to evaporate after 43.5 s (Holborn *et al.*, 2020). We simulate this release by employing the film boiling correlation for H_2 and variable ground properties for dry sand. Our model overestimates the radius and the time until complete boil-off. Since the upstream pressure exceeded atmospheric pressure, flashing is expected. However, this phenomenon was not considered in the calculations to ensure a conservative estimation of the maximum pool radius. Therefore, the discrepancy in the radius could be due to an actual liquid spill rate that was lower than reported. E.g., 41 % flashing was assumed by Verfondern and Dienhart (1997).

Once the liquid forms a pool, multiple reasons may cause overestimation of radius and boil-off time. The bottom friction modelled by the Manning coefficient n in Eqs. (4) and (5) may be larger than expected. However, the pool radius is not particularly sensitive to changes in n for such rapid spills. Next, underestimation of the heat flux could be a factor. However, as is later shown in Figs. 9a and 9b for LH_2, even in the limit of perfect thermal contact, the behaviour remains similar. Larger thermal conductivity or moisture content could contribute to reducing the radius and boil-off time, but to get a significant change in radius, nonphysical values of the thermal-transport properties have to be used. In this NASA test, the trajectory of LH_2 was directed towards a deflection plate prior to reaching the ground. When 30 % to 40 % of the liquid mass flashes, the volume increases about 20 times. This would lead to a significant increase in the velocity. With a high-velocity impact, significant splashing is expected, which could be a large source of evaporation when droplets mix with the warm air. Detailed modelling of the impact zone including splashing, which our tool does not directly account for, would require a more sophisticated multiphase 3D CFD model. Additionally, measurement uncertainty, particularly of the spill radius, could play a role.

Holborn *et al.* (2020) utilized the FLACS pool model and found relatively good agreement with the radius reported in NASA Test 6. However, this was done with wet coarse sand as substrate, for which they selected a thermal conductivity of 3.72 W/m K and thermal diffusivity of $1.45 \cdot 10^{-6}$ m²/s. For dry sand, which better replicates the experimental conditions, our model predicts a thermal conductivity of 0.94 W/m K and thermal diffusivity of $4.88 \cdot 10^{-7}$ m²/s at 0 °C. Hence, the thermal conductivity used by Holborn *et al.* (2020) is about 400 % higher than for dry sand.

To compare the results from FLACS with ours, we employ the same spill zone and constant thermal properties in the ground, along with the same simplification of perfect thermal contact. Moreover, following Holborn *et al.* (2020), we linearize the ground heat flux in Eq. (13) for $t_w < 4$ s. The maximal pool radius differs from that obtained by FLACS by less than 5 %, but the time until complete boil-off is 10 % longer. A different definition of what is regarded as dry ground (see "dry tolerance" in Table 1) may contribute to explain the latter. Additionally, the larger grid spacing used by Holborn *et al.* (2020) may account for the minor discrepancies in radius. The smaller maximal radius assuming different constant thermal properties demonstrates that the estimate of thermal properties in the ground significantly affects the predicted size and evaporation rate of cryogenic pools. The high thermal conductivity used by Holborn *et al.* (2020) may serve to compensate for the effects of flashing and splashing, and explain the difference between the red and black lines in Fig. 5.

3.2. Effect of substrate variations and thermal-transport modelling choices

In the following subsections we investigate the effect changing the substrate, different treatment of thermal properties (temperature dependent vs. constant) and the effect of the solid-to-liquid heat-transfer model used. As a base case we use the NASA Test 6 (Witcofski and Chirivella, 1984) described in Sec. 1, and do variations on this case. The base case thus corresponds to the validation case used in Subsection 3.1.2, corresponding to the red line in Fig. 5. We use the same mass flow rate, for both H_2 and NH_3 spills, and consider both wet and dry sand as substrate. Subsequently, we consider the effect of moisture in concrete. The main cases are summarized in Table 3, in which Cases A–F are axisymmetric releases inside a spill zone having radius 0.75 m with duration 38 s and spill rate
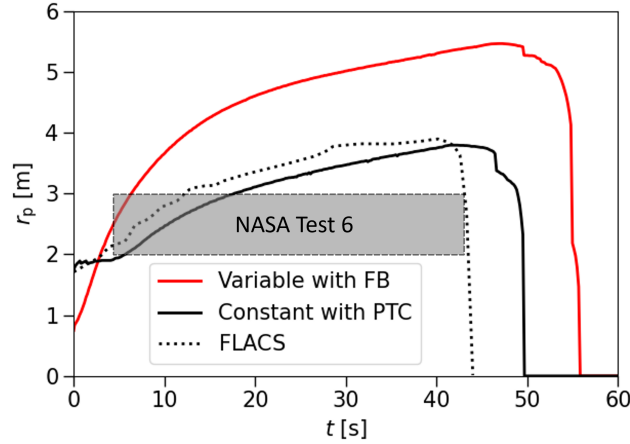
Figure 5: The grey shaded area depicts the experimentally reported pool radius in NASA Test 6. The red line indicates the radius calculated by assuming variable thermal properties and film boiling (FB). The full black line was calculated by assuming perfect thermal contact (PTC) and constant thermal properties to be comparable to Holborn *et al.* (2020) (dotted line).
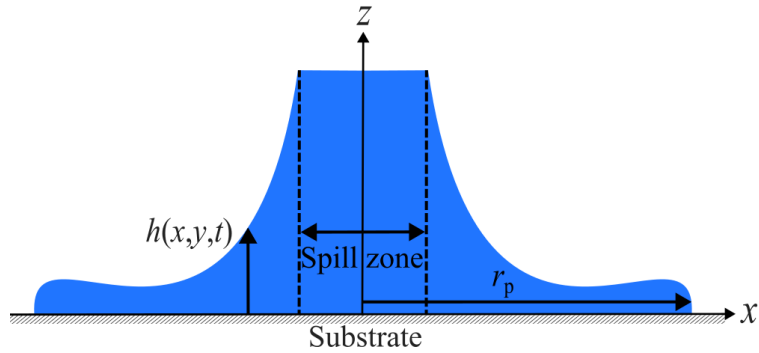
Figure 6: Sketch of an axisymmetric evaporating spill centred at $(x, y) = (0, 0)$ with radius r_p where the spill height $h(x, y, t) = h(r, t)$.

$\dot{m}_\ell = 9.5$ kg/s. This is illustrated in Fig. 6. Finally, we consider a more complex Case X to showcase the versatility of the tool.

3.2.1. Cases A and B: Constant vs. variable thermal substrate properties

The standard approach used in the literature to determine the pool size and evaporation rate for cryogenic liquids is to assume temperature-independent (constant) thermal properties in the ground (Holborn *et al.*, 2020; Verfondern and Dienhart, 1997). To check the validity of this assumption for spills of LH_2 and LNH_3 on dry sand, we have compared the pool radius and evaporation rate for spill Cases A and B. The constant substrate properties are set equal to the properties of dry sand at $T = 10\,°C$. The boiling correlations in Eqs. (20) and (26) are employed for LH_2 and LNH_3, respectively. As seen in Figs. 2a and 2b, there are large variations in thermal properties for the temperatures relevant for LH_2. Thus one could expect a significant impact on the LH_2 case, and less so for the LNH_3 case. However, for dry sand, Figs. 7a and 7b show only insignificant differences in both radius and evaporation rate for constant and variable ground properties for LH_2. We have verified that the same is also the case for LNH_3.

We now switch the substrate to wet sand and extend the LH_2 spill duration to 900 s. The extended spill duration causes more cooling of the ground which increases the effect of variable thermal

Table 3: Spill cases with different substrates and their thermal properties. The right-most column indicates whether boiling correlations for film and nucleate boiling are employed or if perfect thermal contact is assumed.

Case	Substrate	Properties	Boiling
A	Dry sand	Variable	Film/Nucleate
B	Dry sand	Constant	Film/Nucleate
C	Dry sand	Variable	Perfect contact
D	Wet sand	Variable	Film/Nucleate
E	Dry concrete	Variable	Film/Nucleate
F	Wet concrete	Variable	Film/Nucleate
X	Dry concrete and wet sand	Variable	Nucleate

properties. Instead of selecting the thermal properties at the initial ground temperature, $T_g^0 = 10\,°C$, the constant thermal properties are set equal to the thermal properties of the ground at $T = -1\,°C$. This choice is made since cooling to the freezing point is fast, and most of the heat conduction happens through soil at sub-zero temperatures. Evaluating the thermal properties at the initial temperature can lead to an underestimation of heat conduction (see Fig. 2a). The latent heat from the freezing of ground moisture is accounted for heat in c_p^{eff} in all scenarios, so this quantity is never fully constant.

The resulting radius and evaporation rate can be seen in Figs. 8a and 8b, where we observe similar time until complete boil-off, but smaller radius for variable thermal properties. However, the difference in maximal radius is less than 12 %. This result can be explained by the opposing effects of increasing thermal conductivity and decreasing specific heat capacity as a function of decreasing temperature. Therefore, constant thermal properties may be sufficient, provided their values are evaluated at an appropriate temperature. There may, however, be substrates with properties that do not facilitate such a procedure.

3.2.2. Cases A and C: Perfect thermal contact vs. boiling correlations

A common simplification practice in the literature is the assumption of perfect thermal contact between the ground and the liquid (Holborn *et al.*, 2020; Verfondern and Dienhart, 1997). This gives the maximal possible heat flux between the liquid and the ground. However, in reality, there will be a finite temperature difference between the surface and the evaporating liquid, where the heat flux is typically described by a boiling correlation for the relevant boiling regime. For a large temperature difference, typically the case for LH_2, the heat transfer happens through film boiling, having an insulating vapour film between the substrate and the liquid. On the other hand, for LNH_3, the heat transfer is typically within the nucleate boiling regime in which bubbles form at and separate from the ground surface. To account for the different boiling regimes that LH_2 and LNH_3 experience, we employ the boiling correlations in Eqs. (20) and (26), respectively.

The difference between assuming perfect thermal contact and accounting for the boiling regimes is displayed in Figs. 9a and 9b where spill Cases A and C for LH_2 are compared. Perfect thermal contact yielded a higher initial evaporation rate, and the spill evaporated faster. However, with time, the evaporation rates of the two cases approach each other. This shows that the ground's thermal conductivity is a primary factor limiting evaporation once the top layer of the ground has cooled. Hence, the simulations of short-duration spills are more affected by the simplifying assumption of perfect thermal contact.

As seen in Figs. 9c and 9d, the predicted behaviour was similar for LNH_3, albeit with a considerably longer time to complete boil-off, and hence, a larger absolute difference in boil-off time between the cases of perfect thermal contact and nucleate boiling. Despite the marginal differences in radius and evaporation rate, we observed a notable difference in the temperature profiles in the ground. This implies that large differences in temperature profiles do not necessarily give rise to large differences in
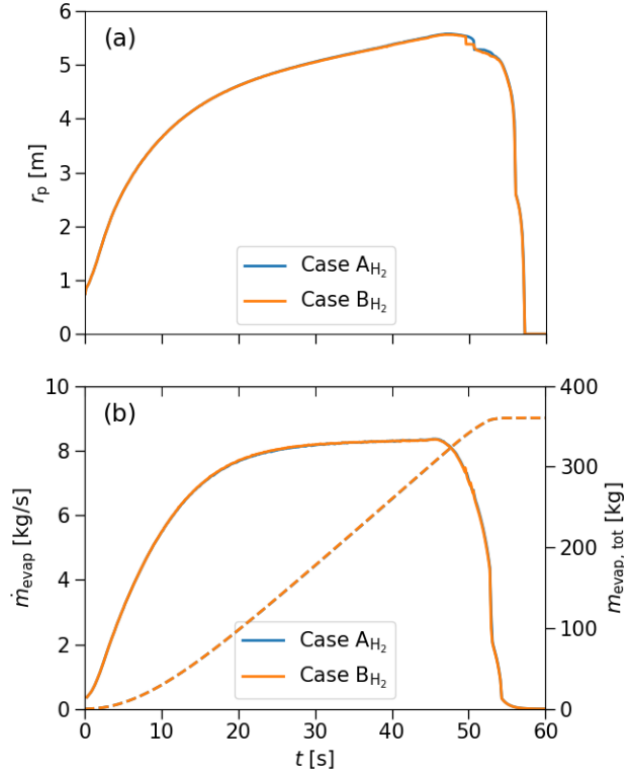
Figure 7: Release cases A and B with LH$_2$. (a) Pool radius. (b) Evaporation rate (full lines) on left second axis and total evaporated mass (dashed lines) on right second axis.

radius and evaporation rate.

3.2.3. Cases A, D, E and F: Dry vs. wet substrate

In the following, we study the effect of ground moisture on radius, evaporation rate and temperature profiles in the ground. Spill Cases A and D are compared in Fig. 10a which shows that for LH$_2$ the pool radius will be smaller for wet saturated sand compared to dry sand. This is reflected in a higher evaporation rate for wet sand in Fig. 10b.

As expected, we observe the same behaviour for LNH$_3$ in Figs. 10c and 10d, but with a significantly more pronounced difference in radius, evaporation rate and time before complete boil-off. The time before complete boil-off was one third for wet sand compared to dry sand.

The large differences between wet and dry sand for LNH$_3$ seen in Figs. 10c and 10d are mainly explained by the release of heat associated with freezing of ground moisture. This in turn maintains a larger temperature difference $\Delta T_{g\ell}$, which in turn causes a higher heat flux from the ground. Additionally, the increase in thermal conductivity λ_g for wet saturated sand may enhance the evaporation compared to dry sand. For LNH$_3$, the ground was maximally cooled to $-27\,°C$ for wet saturated sand, while for LH$_2$ it was maximally cooled to $-98\,°C$. Hence, for LH$_2$, the relative contribution from cooling is higher, and thus the latent heat is less significant.

LNH$_3$ on concrete: Concrete is often used as substrate, both for storage of LNH$_3$ and LH$_2$, and in experiments. Thermal properties of concrete are plotted in Figs. 2a and 2b, but data are only at temperatures relevant to LNH$_3$ spills. The resulting radius and evaporation rate for spill Cases E and F are given in Figs. 11a and 11b. Compared to dry concrete, the time until complete boil-off is one third shorter for concrete that was first dried and then wetted (i.e., rewetted). This illustrates again that evaporation rates for dry and wet substrates are significantly different, and must be accounted for

15
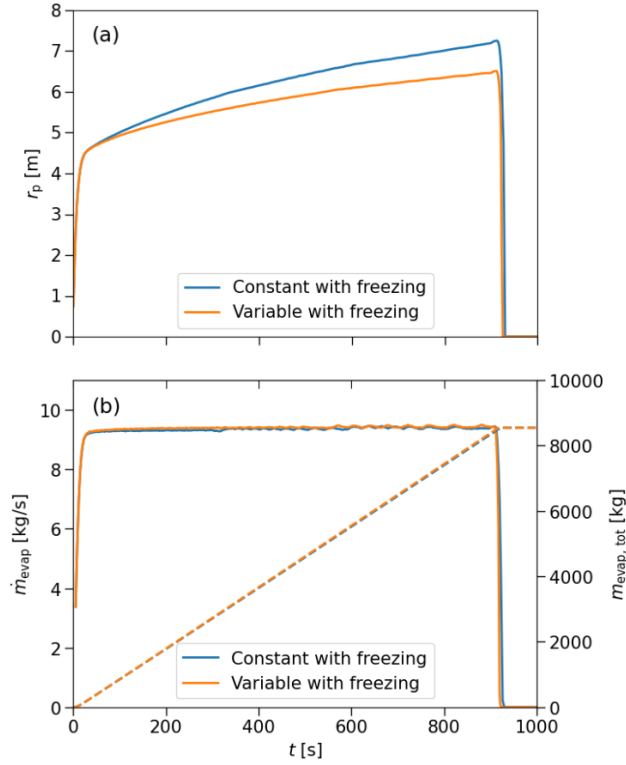
Figure 8: Continuous axisymmetric release of LH$_2$ on wet sand over 1200 s with spill rate $\dot{m}_\ell = 9.5$ kg/s inside a radius of 0.75 m. (a) Pool radius. (b) Evaporation rate (full lines) on left second axis and total evaporated mass (dashed lines) on right second axis. Plotted for constant properties at $T = -1\,°\text{C}$ (blue) and variable thermal properties (orange). Freezing of ground moisture is accounted for in both cases.

when performing hazard and operability studies.

3.2.4. Case X: Complex case

Finally, as a demonstration of the tool, showing its versatility, we simulate a continuous time-dependent spill of LNH$_3$ with mass spill rate (kg/s) $\dot{m}_\ell = 15 - 0.25t$ inside a rectangular domain with an initial velocity $u_0 = 1$ m/s, see Fig. 12. This is similar to the release from a non-pressurized storage tank. The spill is constrained by a wall for $x \leq -2$ m. Two obstacles are included, serving as pillars holding up a roof between the wall and the pillars. The substrate is dry concrete below the roof and wet saturated sand outside the roof. The height and local evaporation rate at $t = 10$ s are shown in Figs. 13a and 13b. Both variable ground properties and the boiling correlation in Eq. (26) have been employed. Here we observe how wet saturated sand causes a higher local evaporation rate compared to dry concrete.

This demonstration case shows that the model can be applied to complex geometries relevant to real storage and transport infrastructure. Such cases could prove important both for detailed analysis of the development and extent of the cold spill, and as input to improved analysis of the formation and spread of the hazardous cloud.

16
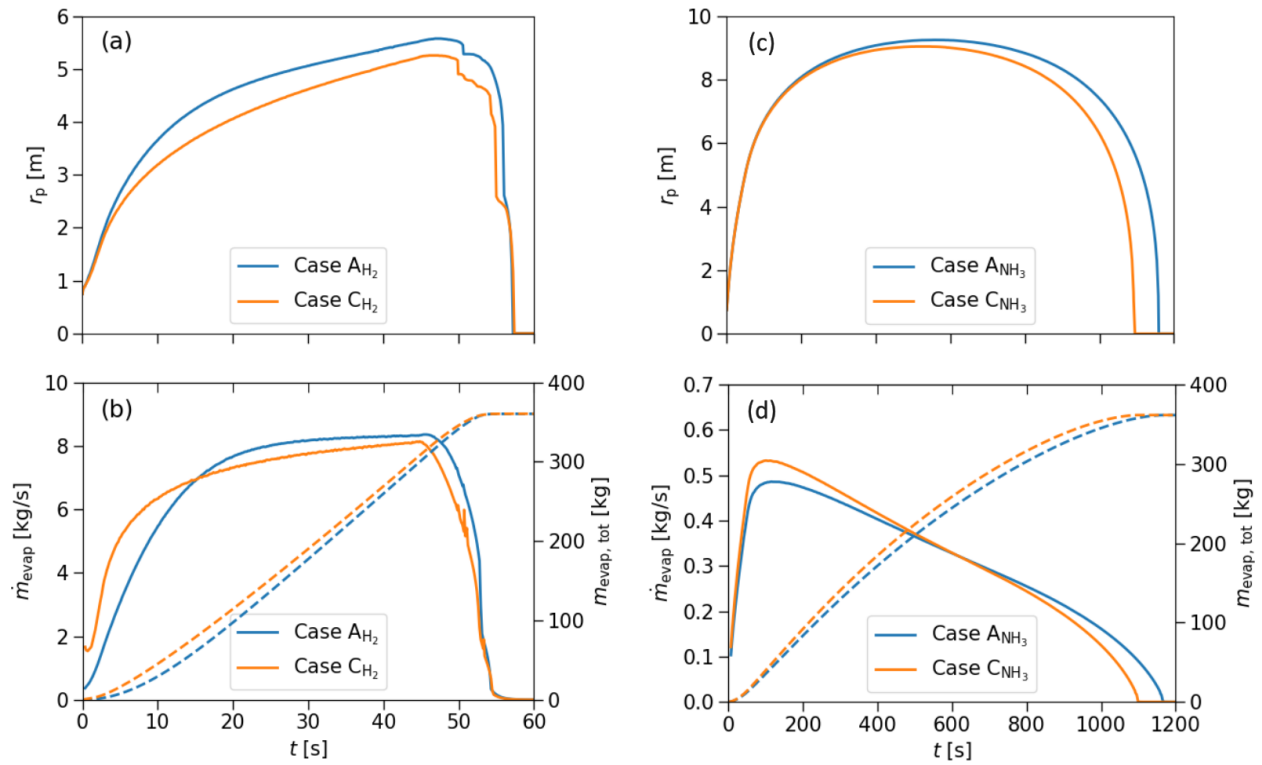
Figure 9: Release Cases A and C for LH$_2$ (left column) and LNH$_3$ (right column). (a) and (c) Pool radius. (b) and (d) Evaporation rate (full lines) on left second axis and total evaporated mass (dashed lines) on right second axis.

4. Conclusions

In this work, a new, flexible tool has been developed to simulate the spreading and continuous evaporation of cryogenic liquids, such as LH$_2$ and LNH$_3$, on land. The tool can account for various spill and substrate details, including transient spill rates, the initial momentum of the spill, the topography of the ground, obstructions, and temperature-dependent thermal properties of the substrate.

Exploiting the fact that the heat conduction is mainly vertical and initiated by the spill's wetting, we have implemented the substrate heat conduction as a pre-processing step, reducing computational times significantly.

The tool's validation against experiments highlighted the importance of understanding the thermal properties of the ground. Moreover, the constant-thermal-properties assumption was found reasonable for both LH$_2$ and LNH$_3$ spills, provided the substrate thermal properties are evaluated at frozen-soil temperatures and that the latent heat of substrate moisture is accounted for. Similarly, assuming perfect thermal contact or using a boiling correlation did not give significant differences in the spill-evaporation development. Both these assumptions should be checked if other substrates are considered, or for long-duration spills.

Furthermore, the effect of ground moisture was investigated. The water content in the substrate was found to have a significant impact on the spill spread and evaporation. The effect was found to be particularly pronounced for LNH$_3$, with a relative increase in peak evaporation rate of 1.5 or 3 when concrete or sand was wetted, respectively. This highlights the importance of accounting for ground moisture when predicting the size and evaporation rate of cryogenic pools. These findings can inform more accurate hazard and operability studies for cryogenic storage and handling facilities.

17
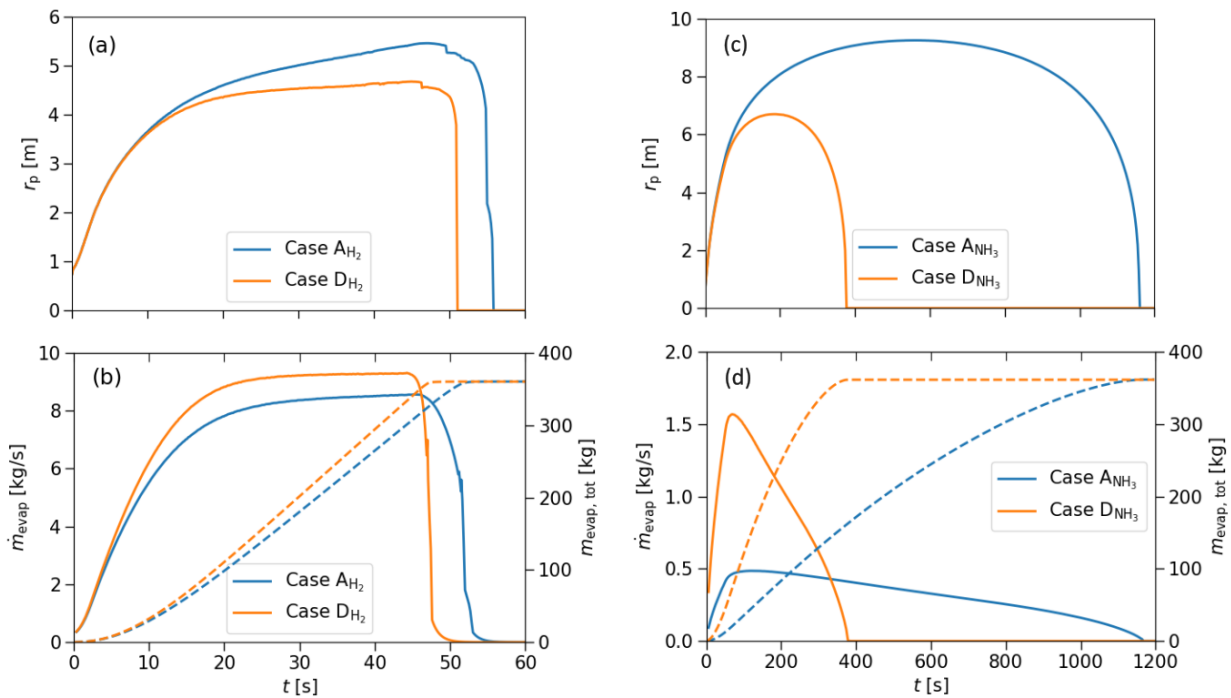
Figure 10: Release Cases A and D for LH_2 (left column) and release Cases A and D for LNH_3 (right column). (a) and (c) Pool radius. (b) and (d) Evaporation rate (full lines) on left second axis and total evaporated mass (dashed lines) on right second axis.

References

Aaneby, J., Gjesdal, T., Voie, Ø. A., 2021. *Large scale leakage of liquid hydrogen (LH2) – tests related to bunkering and maritime use of liquid hydrogen.* FFI-Report 20/03101, Norwegian Defence Research Establishment. URL `https://www.ffi.no/en/publications-archive/large-scale-leakage-of-liquid-hydrogen-lh2-tests-related-to-bunkering-and-maritime-use-of-liquid-hydrogen`.

Baldwin, M., Ghavami, A., Ghiaasiaan, S. M., Majumdar, A., Apr. 2021. Pool boiling in liquid hydrogen, liquid methane and liquid oxygen: A review of available data and predictive tools. *Cryogenics* 115, 103240. ISSN 0011-2275. doi:10.1016/j.cryogenics.2020.103240.

Berstad, D., Gardarsdottir, S., Roussanaly, S., Voldsund, M., Ishimoto, Y., Nekså, P., 2022. Liquid hydrogen as prospective energy carrier: A brief review and discussion of underlying assumptions applied in value chain analysis. *Renewable and Sustainable Energy Reviews* 154, 111772. ISSN 1364-0321. doi:10.1016/j.rser.2021.111772.

Carnahan, E., Wolfenbarger, N. S., Jordan, J. S., Hesse, M. A., Jun. 2021. New insights into temperature-dependent ice properties and their effect on ice shell convection for icy ocean worlds. *Earth and Planetary Science Letters* 563, 116886. ISSN 0012-821X. doi:10.1016/j.epsl.2021.116886.

Clawpack Development Team, 2022. Clawpack software v5.9.0. doi:10.5281/zenodo.7026044.

Côté, J., Konrad, J.-M., Apr. 2005a. A generalized thermal conductivity model for soils and construction materials. *Canadian Geotechnical Journal* 42 (2), 443–458. ISSN 0008-3674. doi:10.1139/t04-106.

Côté, J., Konrad, J.-M., Feb. 2005b. Thermal conductivity of base-course materials. *Canadian Geotechnical Journal* 42 (1), 61–78. ISSN 0008-3674. doi:10.1139/t04-081.

Dahmani, L., Khenane, A., Kaci, S., Sep. 2007. Behavior of the reinforced concrete at cryogenic temperatures. *Cryogenics* 47 (9), 517–525. ISSN 0011-2275. doi:10.1016/j.cryogenics.2007.07.001.
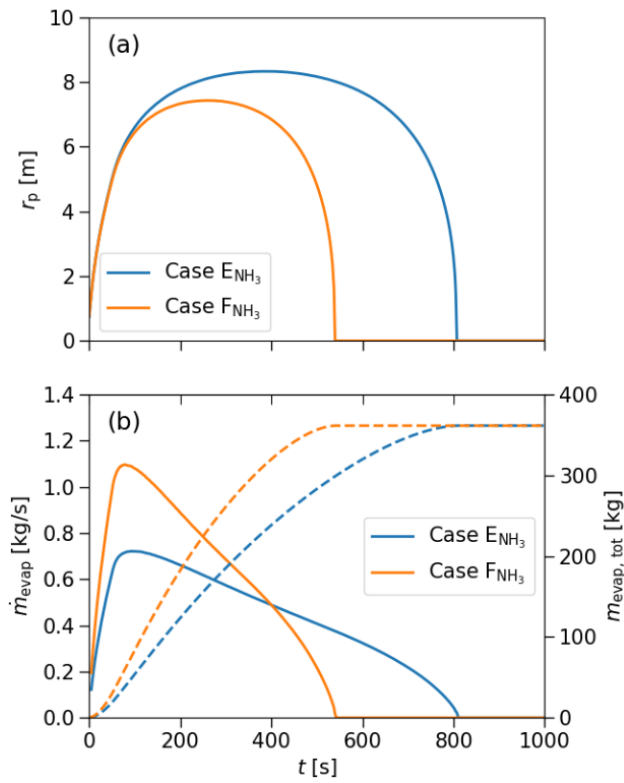
Figure 11: Release Cases E and F for LNH$_3$. (a) Pool radius. (b) Evaporation rate (full lines) on left second axis and total evaporated mass (dashed lines) on right second axis.
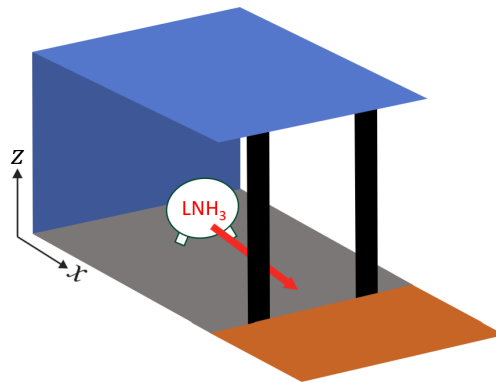
Figure 12: Sketch of complex Case X where LNH$_3$ is released on dry concrete (grey) under a roof (blue) and subsequently reaches wet saturated sand (brown). A wall (blue) and pillars (black) constrain the spill.
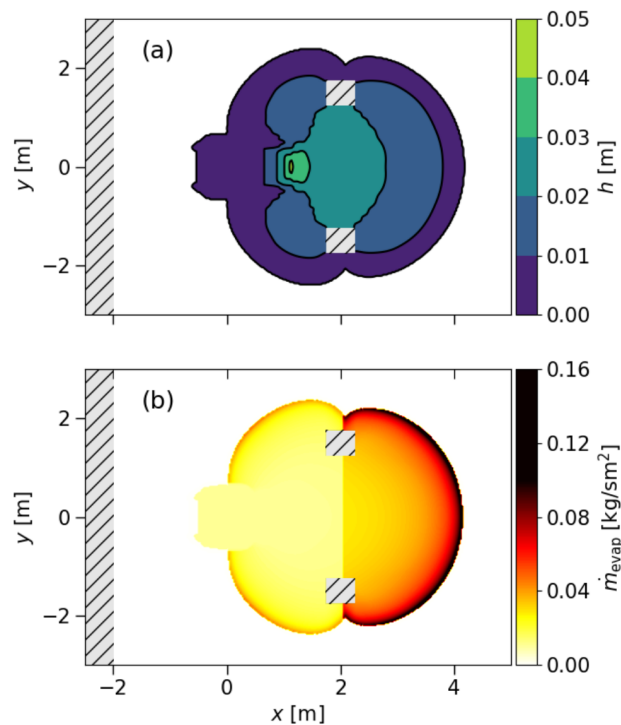
Figure 13: Top-down view of release Case X (Fig. 12). Time-dependent continuous spill of LNH$_3$ at a rate (kg/s) $\dot{m}_\ell = 15 - 0.25t$ inside a rectangular domain of size $x \times y = 1\,\text{m} \times 0.75\,\text{m}$ with initial velocity $u_0 = 1\,\text{m/s}$. Obstacles are displayed in hatched grey. The substrate is dry concrete ($x \leq 2.1$ m) and wet saturated sand ($x \geq 2.1$ m). (a) Height of spill at $t = 10$ s. (b) Local evaporation rate at $t = 10$ s.

Dharmavaram, S., Carroll, M. J., Lutostansky, E. M., McCormack, D., Chester, A., Allason, D., 2023. Red Squirrel Tests: Air Products' ammonia field experiments. *Process Safety Progress* 42 (3), 481–498. ISSN 1547-5913. doi:10.1002/prs.12454.

Dincer, I., Zamfirescu, C., 2015. Appendix B Thermophysical Properties of Water. In: *Drying Phenomena*, John Wiley & Sons, Ltd, pp. 457–459. ISBN 978-1-118-53489-2. doi:10.1002/9781118534892.app2.

Grønli, M. S., Skarsvåg, H. L., Munkejord, S. T., 2024. Cryogenic pool spreading and vaporization. GitHub repository. `https://github.com/martinspgronli/cryogenic_pool_spreading_and_vaporization`. Accessed: 2024-11-14.

Hall, J., 2014. *Ignited releases of liquid hydrogen.* Tech. Rep. RR987, Health and Safety Laboratory. URL `https://www.hse.gov.uk/Research/rrhtm/rr987.htm`.

Harvey, A., 2019. Properties of Ice and Supercooled Water. In: *CRC Handbook of Chemistry and Physics*, CRC Press. URL `https://tsapps.nist.gov/publication/get_pdf.cfm?pub_id=926353`.

Holborn, P. G., Benson, C. M., Ingram, J. M., Sep. 2020. Modelling hazardous distances for large-scale liquid hydrogen pool releases. *International Journal of Hydrogen Energy* 45 (43), 23851–23871. ISSN 0360-3199. doi:10.1016/j.ijhydene.2020.06.131.

Jackson, H., Dec. 2019. pyPDE. Python library v0.32.1. URL `https://pypi.org/project/PyPDE/`.

Kadoya, K., Matsunaga, N., Nagashima, A., Oct. 1985. Viscosity and Thermal Conductivity of Dry Air in the Gaseous Phase. *Journal of Physical and Chemical Reference Data* 14 (4), 947–970. ISSN 0047-2689. doi:10.1063/1.555744.

Ketcheson, D. I., Parsani, M., LeVeque, R. J., 2013. High-order Wave Propagation Algorithms for Hyperbolic Systems. *SIAM Journal on Scientific Computing* 35 (1), A351–A377. doi:10.1137/110830320.

Klimenko, V. V., Shelepen, A. G., Oct. 1982. Film boiling on a horizontal plate - a supplementary communication. *International Journal of Heat and Mass Transfer* 25 (10), 1611–1613. ISSN 0017-9310. doi:10.1016/0017-9310(82)90042-4.

Lemmon, E. W., Bell, I. H., Huber, M. L., McLinden, M. O., 2024. Thermophysical Properties of Fluid Systems. In: Linstrom, P. J., Mallard, W. G. (Eds.), *NIST Chemistry WebBook, NIST Standard Reference Database Number 69*, National Institute of Standards and Technology. doi:10.18434/T4D303.

Lemmon, E. W., Jacobsen, R. T., Penoncello, S. G., Friend, D. G., May 2000. Thermodynamic Properties of Air and Mixtures of Nitrogen, Argon, and Oxygen From 60 to 2000 K at Pressures to 2000 MPa. *Journal of Physical and Chemical Reference Data* 29 (3), 331–385. ISSN 0047-2689. doi:10.1063/1.1285884.

Mangala Gitushi, K., Blaylock, M., Hecht, E. S., Jan. 2023. Simulations for Planning of Liquid Hydrogen Spill Test. *Energies* 16 (4), 1580. ISSN 1996-1073. doi:10.3390/en16041580.

McMasters, S., Fox, S., 2020. Jack Rabbit III Initiatives. U.S. Department of Homeland Security. Seminar presentation.

https://www.cisa.gov/sites/default/files/publications/2020-seminars-jack-rabbit-III-508.pdf.

Mostinski, I., 1963. Application of the rule of corresponding states for calculation of heat transfer and critical heat flux. *Teploenergetika* 4 (4), 66–71.

Sciance, C. T., 1966. *Pool boiling heat transfer to liquefied hydrocarbon gases*. Ph.D. thesis, The University of Oklahoma. URL https://core.ac.uk/download/pdf/215277056.pdf.

Simoncelli, M., Mauri, F., Marzari, N., Jun. 2023. Thermal conductivity of glasses: first-principles theory and applications. *npj Computational Materials* 9 (1), 1–22. ISSN 2057-3960. doi:10.1038/s41524-023-01033-4.

Skarsvåg, H. L., Fyhn, E. H., Aasen, A., 2024. Influence of ammonia-water fog formation on ammonia dispersion from a liquid spill. *Journal of Loss Prevention in the Process Industries* 92, 105446. ISSN 0950-4230. doi:10.1016/j.jlp.2024.105446.

Spiegler, P., Hopenfeld, J., Silberberg, M., Bumpus Jr, C., Norman, A., 1963. Onset of stable film boiling and the foam limit. *International Journal of Heat and Mass Transfer* 6 (11), 987–989. doi:10.1016/0017-9310(63)90053-X.

Statharas, J. C., Venetsanos, A. G., Bartzis, J. G., Würtz, J., Schmidtchen, U., Oct. 2000. Analysis of data from spilling experiments performed with liquid hydrogen. *Journal of Hazardous Materials* 77 (1), 57–75. ISSN 0304-3894. doi:10.1016/S0304-3894(00)00252-1.

The Engineering ToolBox, 2004. Manning's Roughness Coefficients. Webpage. https://www.engineeringtoolbox.com/mannings-roughness-d_799.html. URL https://www.engineeringtoolbox.com/mannings-roughness-d_799.html. Accessed: 2022-12-20.

van den Bosch, C. J. H., Weterings, R. A. P. M., 2005. *Methods for the Calculation of Physical Effects: Due to Releases of Hazardous Materials, Liquids and Gases: Yellow Book*. Ministerie van Volkshuisvesting en Ruimtelijke Ordening (VROM).

van der Spek, M., Banet, C., Bauer, C., Gabrielli, P., Goldthorpe, W., Mazzotti, M., Munkejord, S. T., Røkke, N. A., Shah, N., Sunny, N., Sutter, D., Trusler, J. M., Gazzani, M., 2022. Perspective on the hydrogen economy as a pathway to reach net-zero CO_2 emissions in Europe. *Energy & Environmental Science* 15 (3), 1034–1077. doi:10.1039/D1EE02118D.

Verfondern, K., Dienhart, B., Jul. 1997. Experimental and theoretical investigation of liquid hydrogen pool spreading and vaporization. *International Journal of Hydrogen Energy* 22 (7), 649–660. ISSN 0360-3199. doi:10.1016/S0360-3199(96)00204-2.

Wilhelmsen, Ø., Aasen, A., Skaugen, G., Aursand, P., Austegard, A., Aursand, E., Gjennestad, M. A., Lund, H., Linga, G., Hammer, M., Apr. 2017. Thermodynamic Modeling with Equations of State: Present Challenges with Established Methods. *Industrial & Engineering Chemistry Research* 56 (13), 3503–3515. ISSN 0888-5885. doi:10.1021/acs.iecr.7b00317.

Willoughby, D., Royle, M., 2014. *Releases of unignited liquid hydrogen*. Tech. Rep. RR986, Health and Safety Laboratory. URL https://www.hse.gov.uk/research/rrhtm/rr986.htm.

Witcofski, R. D., Chirivella, J. E., Jan. 1984. Experimental and analytical analyses of the mechanisms governing the dispersion of flammable clouds formed by liquid hydrogen spills. *International Journal of Hydrogen Energy* 9 (5), 425–435. ISSN 0360-3199. doi:10.1016/0360-3199(84)90064-8.